Astron. Astrophys. 347, 640–649 (1999)

ASTRONOMY
AND
ASTROPHYSICS

PRONAOS observations of MCLD 123.5 + 24.9: cold dust in the Polaris cirrus cloud

J.P. Bernard[1], **A. Abergel**[1], **I. Ristorcelli**[2], **F. Pajot**[1], **J.P. Torre**[3], **F. Boulanger**[1], **M. Giard**[2], **G. Lagache**[1], **G. Serra**[2], **J.M. Lamarre**[1], **J.L. Puget**[1], **F. Lepeintre**[1], **and L. Cambrésy**[4]

[1] IAS, bâtiment 121, Campus d'Orsay, F-91405 Orsay Cedex, France
[2] CESR, 9 Avenue du Colonel Roche, B.P. 4346, F-31029 Toulouse, France
[3] SA, UPR-CNRS, Verrières-le Buisson, France
[4] DESPA, Observatoire de Paris, 5 Place Jules Janssen, F-92195 Meudon Cedex, France

Received 7 January 1999 / Accepted 18 March 1999

Abstract. We present submillimeter observations between 200 and $600\,\mu$m obtained with the French balloon-borne instrument SPM/PRONAOS toward the high latitude cirrus cloud $\mathrm{MCLD}\,123.5+24.9$ in the Polaris Flare. These sensitive measurements allow for the first time to study in details the submillimeter dust emission of cirruses at the arc minute scale. The extended cirrus as well as a compact condensation already identified as an $\mathrm{NH_3}$ core are well detected in the four photometric channels of the instrument. We also present preliminary results of observations of the same region at $150\,\mu$m obtained with PHOT on board the ISO satellite. The data are consistent with emission from cold dust at 13 K with a steep dust emissivity index of $\beta = 2.2$ for the extended cirrus. This value is consistent with, although slightly higher than the one used to describe the FIRAS data at high latitude ($\beta = 2.0$). It is compatible with recent laboratory measurements for amorphous silicates at low temperature which indicate $\beta > 2.0$. We show that the low value of the dust temperature for the extended cirrus cannot be explained by extinction from the surrounding medium and/or internal extinction in the cloud.

We propose that the optical properties of dust in regions such as the Polaris cirrus, which exhibit large $100\,\mu$m excess over their $60\,\mu$m emission, are modified compared to those prevailing in the general diffuse interstellar medium in the Galaxy. This change in the optical properties of large grains is likely connected to the coagulation of smaller dust particles on large size grains.

Key words: ISM: clouds – ISM: dust, extinction – ISM: individual objects: MCLD 123.5+24.9 – infrared: ISM: continuum – submillimeter

1. Introduction

It is now well established that, on large scales, cold dust exist in high latitude cirrus clouds. Boulanger et al. (1996) have shown that the FIRAS/COBE (angular resolution 7°) emission at high latitude ($|b| > 20°$) can be well represented by a grey body law with an average dust temperature $T_\mathrm{d} = 17.5\,\mathrm{K}$ assuming an emissivity index β=2. Note that the value for β could not be precisely derived using the FIRAS data alone. Using the same dataset, Reach et al. (1995) evidenced a very cold component ($T_\mathrm{d} = 5-7\,\mathrm{K}$) which they claimed is present not only along the galactic ridge but also at high Galactic latitudes. However, their analysis was hampered by the existence of an isotropic Far IR extra-galactic Background (FIRB) which was since evidenced by Puget et al. (1996). Lagache et al. (1998) have shown that the very cold component is in fact greatly reduced when the FIRB is included in the analysis and can even be completely removed at high galactic latitudes, within the uncertainties on the FIRB intensity. In their analysis, they have shown that, at the large angular scales observed by FIRAS, the histogram of the equilibrium temperature of large dust grains exhibits two peaks at $15\,\mathrm{K}$ and $17.9\,\mathrm{K}$ which corresponds to cold molecular clouds and diffuse atomic clouds respectively. The lowest dust temperature for the cirrus component at that scale is $T_\mathrm{d} \simeq 13\,\mathrm{K}$.

At higher angular resolution than FIRAS, the all sky maps of IRAS or DIRBE/COBE (4' and 40' respectively) can be used but the highest wavelength available (100 and $240\,\mu$m respectively) are too low to constrain T_d and β simultaneously. Therefore, little is known about the dust temperature distribution and emissivity law at scales below the DIRBE resolution (0.7°) in cirruses. Note that this information is of prime importance to account accurately for the foreground contamination of future missions aiming at measuring the small scale fluctuations of the cosmological background, such as Planck.

In this paper, we present submillimeter data ($200\,\mu\mathrm{m} < \lambda < 600\,\mu$m) at the 3' scale obtained with the balloon-borne experiment SPM/PRONAOS toward the cirrus $\mathrm{MCLD}\,123.5+24.9$. This cloud is located in a vast region of extended FIR emission, the Polaris Flare, which exhibits a dust temperature ($T_\mathrm{d} = 16.7\,\mathrm{K} \pm 0.14\,\mathrm{K}$ using β=2) at the FIRAS resolution, is significantly lower than for the average cirruses. Similarly, the cirrus $\mathrm{MCLD}\,123.5{+}24.9$ shows a particularly high value of the IRAS I_{100}/I_{60} ratio of 29.5, again much larger than the average value of 3.2 (Lagache et al. 1998). It must be stressed that selecting a

---

Send offprint requests to: J.P. Bernard (bernard@ias.fr) region with such extreme colours tends to maximise the chances of detecting cold dust and that the selected region may therefore not represent the average conditions in cirrus clouds. We centered our observations on a well defined patch of extinction observed in deep B band CCD images of that region (see Fig. 1b) which will be presented in more details by Zagury et al. (1999). In the following, we refer to this object as the $\mathrm{Telephone}$ nebula, owing to the distinctive shape of the extinction region in the B band image (see Fig. 1b).

The large scale $^{12}\mathrm{CO}$(J=1-0) emission of the Polaris Flare has been presented by Heithausen and Thaddeus (1990) and Heithausen et al. (1993) who evidenced a large body of molecular material extending over $\simeq 40^{\circ 2}$ from the tip of the Cepheus Flare (Grenier et al. 1989) toward and beyond the Polaris star. They showed that UBV photometry of stars in this region indicate a distance $< 240\,\mathrm{pc}$ for the flare. The molecular emission of $\mathrm{MCLD}\,123.5 + 24.9$ has been extensively studied by Großmann et al. (1990) (OH, CO and $\mathrm{H_2CO}$ absorption). Their $\mathrm{H_2CO}$ absorption map follows well the overall shape of the IRAS $100\,\mu\mathrm{m}$ emission of the cirrus (see their Fig. 1) and shows the existence of several well defined cores along the cirrus filamentary shape. Großmann and Heithausen (1992) conducted additional observations of a limited region near the strongest of these clumps in several rare isotopes and high dipole moment molecules ($\mathrm{C^{18}O}$(J=1-0 and J=2-1), $^{13}\mathrm{CO}$(J=1-0), $\mathrm{HCO^+}$(J=1-0), HCN and HNC (J=1-0) and $\mathrm{NH_3}$(J,K=1,1 and 2,2)) at higher angular resolution. They detected two well defined $\mathrm{NH_3}$ cores in this region which can also be seen in HNC and $\mathrm{HCO^+}$. The two $\mathrm{NH_3}$ cores happen to correspond exactly to the two ends of the telephone shape seen in B band extinction. In particular, the northern end of the $\mathrm{Telephone}$ nebula, which we observed with SPM corresponds to the $\mathrm{NH_3}$ clump labelled $\mathrm{NH_3}$ -A by Großmann and Heithausen, while the Southern one corresponds to $\mathrm{NH_3 - B}$. For the sake of comparison with molecular data, we will adopt their distance estimate of 200 pc for the extended cirrus $\mathrm{MCLD}\,123.5 + 24.9$. Recently, higher angular resolution molecular observations of the dense $\mathrm{NH_3}$ cores have been presented by Falgarone et al. (1998) as part of an IRAM 30m antenna key program.

We present the SPM data in Sect. 2 and additional recent ISOPHOT observations at $\lambda = 150\,\mu\mathrm{m}$ in Sect. 3. We derive physical parameters for the clouds in Sect. 4 and discuss the results in Sect. 5. Our conclusions are presented in Sect. 6.

2. SPM/PRONAOS observations

The balloon-borne experiment PRONAOS[1] ("PROjet NAtional d'Observation Submilletrique") consist of a gondola hosting a 2m segmented submillimeter telescope. The first flight of the instrument was performed in September 1994 and gave only limited scientific results (see Ristorcelli et al. 1998) due to pointing problems. The observations presented here were obtained during the second flight from Fort-Sumner (NM, USA) on September 22 1996 during which data could be obtained under good conditions for more than 20 hours. The fine pointing of the payload is ensured by a star tracker allowing night and day detection of stars to a relative accuracy of about 5" rms. Details of the gondola stabilisation and pointing are given in Buisson et al. (1997).

The focal plane instrument, SPM ("Spectro Photometre Submillimetrique"), is a submillimeter photometer observing simultaneously in four channels at 200, 260, 360 and $580\,\mu\mathrm{m}$ (effective wavelengths for a ν^2 emissivity grey body spectrum at 30 K) in wide bands ($\Delta\lambda$ =60, 100, 200 and $560\,\mu\mathrm{m}$ respectively). A detailed description of the SPM photometer and the PRONAOS gondola and telescope is given in Lamarre et al. (1994). The beam of the instrument is modulated on the sky with an amplitude of 6.0' at a frequency of 20 Hz using an internal wobbling mirror. Detection is achieved using four bolometers cooled to 0.3 K by two compact, closed cycle $^3\mathrm{He}$ fridges. The FWHM beam size, as measured on a map of Saturn during the flight, is $2'$, $2'$, $2.5'$ and $3.5'$ respectively. The in-flight response of the SPM instrument is measured using an Internal Calibration System (ICS) which is composed of two blackbodies at 310 and 370 K. The differential signal of the ICS is injected at the entrance of the instrument between each observations using a movable mirror. The analysis of this calibration signal (Pajot et al. 1999) over the 21 hours of data taking showed variations of the response lower than 10% in all 4 bands and a relative uncertainty between photometric bands of less than 5%. The absolute calibration of the ICS was checked in flight against a $20' \times 10'$ map of Saturn which we also used to precisely measure the beam shapes in the four bands. The relative flux values in the four bands agree well with the expected spectrum for the planet but is about 15% below the flux level predicted by models of the planet's atmosphere. It is not clear whether the difference reflects an actual calibration trend or uncertainties in the model used to describe Saturn's atmosphere emission (see Pajot et al. 1999 for a full discussion). In the following, we adopt the calibration given by the ICS before and after the observation of the cirrus, without further correction for the discrepancy on Saturn and we quote an absolute uncertainty on the fluxes of 15% and a relative uncertainty between bands of 5%.

We observed a 30' cut across the $\mathrm{MCLD}\,123.5{+}24.9$ cirrus cloud on September 23, for 40 minutes between 9:37 and 10:17 TU at the ceiling altitude of 35 km. The observations where centered on the position of the extinction patch seen at the center of the B band image shown in Fig. 1b at $\alpha_{1950} = 1^{\mathrm{h}}45^{\mathrm{m}}37.87^{\mathrm{s}}$, $\delta_{1950} = 87^{\circ}27'26$" ($l = 123.69^{\circ}$, $b = 24.93^{\circ}$). We obtained 35 scans at a constant elevation of $\simeq 37^{\circ}$ at a speed of 30"/s with a beam modulation distance along the scan direction of 6.0'. Successive scans were separated by 3" in elevation. The resulting pattern observed on the sky is shown in Fig. 1 superposed to the IRAS $100\,\mu\mathrm{m}$ map and a deep B band CCD image of the region. The V-shape is due to the combination of the rotation of the sky during the observations and the slight elevation offset between scans. The star used for pointing is only 1.6° away from the cut center so that pointing errors induced by inaccurate corrections for the swing motion of the gondola were always small ($<$ 7").

---

[1] PRONAOS was built as a national cooperation involving the *Centre National de Recherche Scientifique* (CNRS) and the *Centre National d'Etudes Spatiales* (CNES).

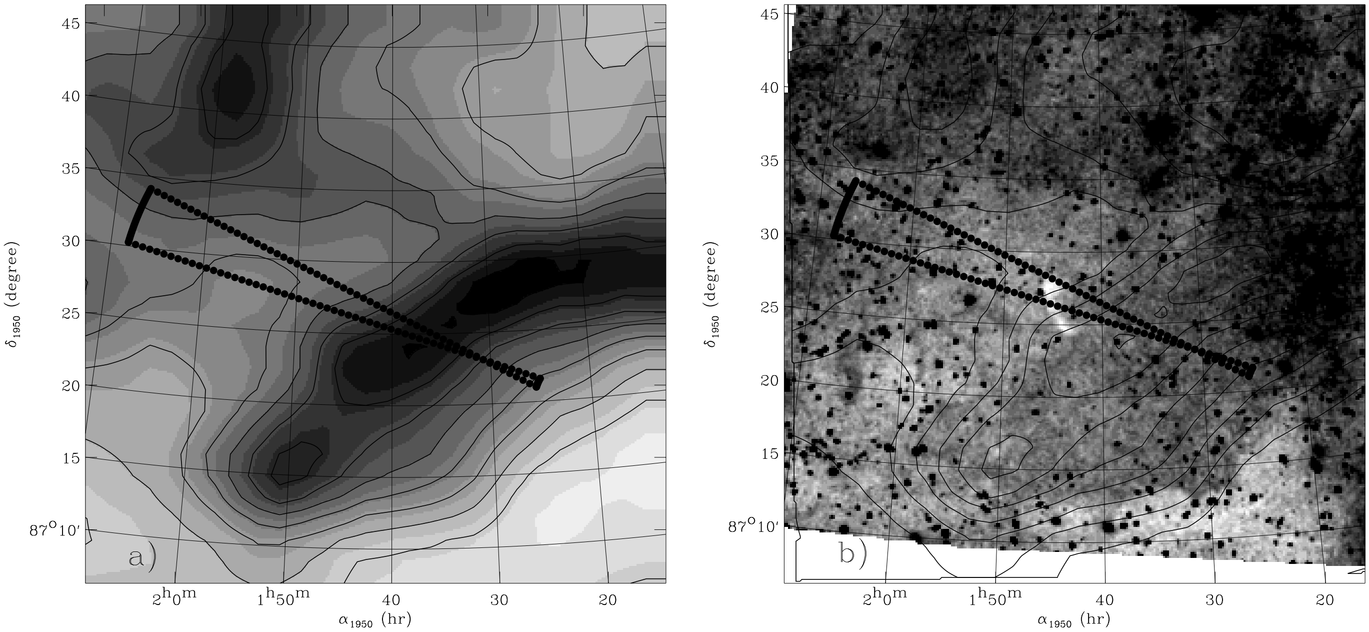

Fig. 1a and b. Sketch of the positions observed with SPM/PRONAOS in the Polaris cirrus cloud overlaid on the IRAS $100\,\mu$m map (**a**) and a deep B band CCD image (**b**) of the region. The $100\,\mu$m levels in both figures start at 6 MJy/sr with an increment of 1 MJy/sr. Note the white region of extinction in the B band image corresponding to the Telephone Nebula.

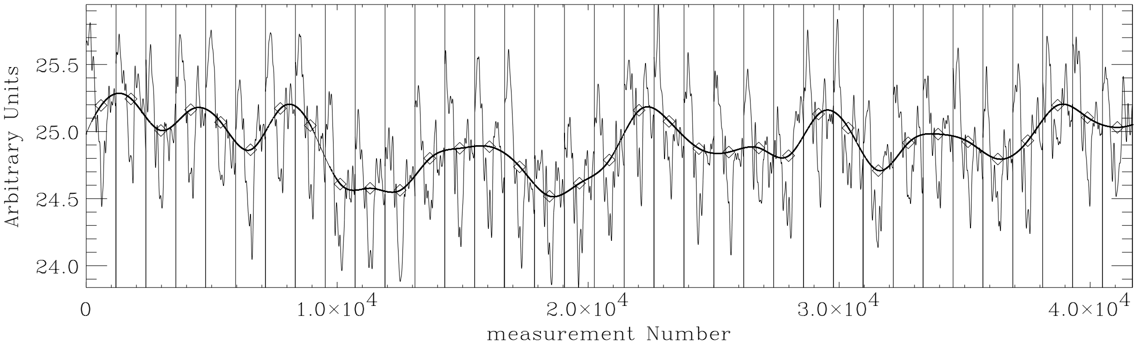

Fig. 2. Temporal signal in the $200\,\mu$m band obtained during the observations of MCLD $123.5 + 24.9$. Vertical lines delimits each of the 25 individual scans through the source. The global spline baseline applied to the data (see text) is also shown.

The data was deglitched using a standard temporal algorithm. The deglitched signal measured in the $200\,\mu$m band for the 35 scans is shown on Fig. 2. A coherent large scale pattern is obvious in all scans. It is also clear that long term fluctuations of the zero level are present in the data. We correct for these by averaging the signal of each scans and globally remove a spline curve constrained on the average points from the raw data. The average values and the resulting baseline used are shown on Fig. 2. The signal averaged over all individual scans is shown in Fig. 3. Compared to the usual baseline procedure which is to remove baselines based on the scan edges on a scan by scan basis, the global spline procedure has the advantage not to constrain to zero the dual beam signal at scan edges. This is important here, since the western part of the cut is not lying on a flat region of the $100\,\mu$m sky (see Fig. 1). The high signal level seen in the averaged scan signal at offset $\simeq -10'$ in Fig. 3 is actually a measure of that emission gradient. The method used latter in the data reduction to deconvolve the signal from the dual beam response (see Sect. 4) forces the edges of scans to be zero, and the above advantage is lost in the restored data. However, we found that the global baseline follows the low frequency variations of the signal more accurately than the usual baseline procedure, leading to more stable results during deconvolution. Fig. 3 shows that the large scale emission of the cirrus is detected in all SPM photometric channels with a shape similar to that of the $100\,\mu$m. In addition to the extended cirrus emission, a point-like source is clearly seen near the center of the cut with the proper beam throw distance. This source corresponds to the Telephone nebula.

3. ISO/PHOT observations

We obtained a map of the region observed with SPM in MCLD $123.5 + 24.9$ at $150\,\mu$m using the PHOT instrument (Lemke et al. 1996) on board the ISO satellite. This obser-

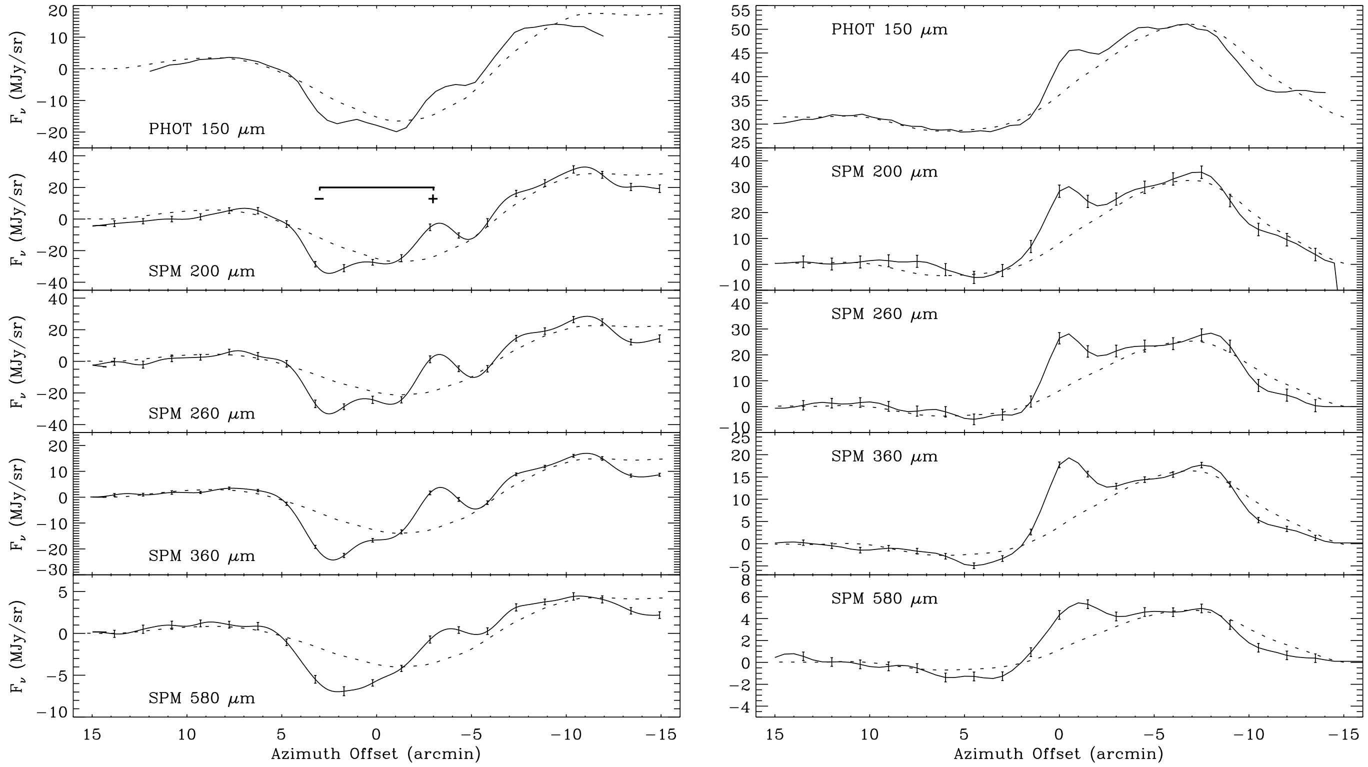

Fig. 3. The left panel shows the average dual beam signal along the 30’ cut observed by SPM and simulated in the PHOT map at $150\,\mu$m (see text). Error bars show the representative rms dispersion between scans ($\pm3\sigma$). The dashed curve shows the simulated IRAS $100\,\mu$m dual beam signal rescaled as described in the text. The amplitude of the beam throw (6’) is also shown. The right panel shows the SPM signal after deconvolution from the dual beam pattern, as well as the signal at the same positions in the PHOT map at $150\,\mu$m. Right ascension along the cut increases to the left.

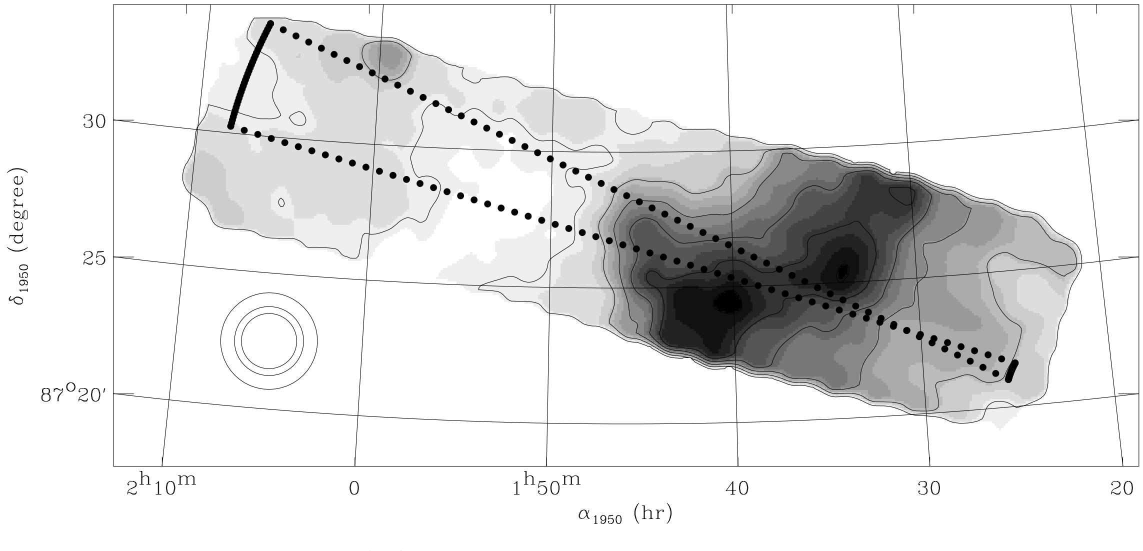

Fig. 4. ISOPHOT map around the Telephone region observed at $150\,\mu$m. The lower contour and contour interval are 30 MJy/sr and 5 MJy/sr respectively. The range of positions observed using SPM is also shown the filled symbols. The beam size of the SPM/PRONAOS photometric channels is also shown.

vation was part of an open time program (COLDCORE, P.I. G. Serra) dedicated to complement SPM observations toward shorter wavelengths. The ISOPHOT map consists of an elongated ($30' \times 5'$) raster with AOT P22 covering precisely the region observed by SPM (see Fig. 4), with some overlap between successive frames. The PHOT data was treated in a standard fashion (deglitching, linearity correction of the ramps, dark current subtraction) using the PHOT Interactive Analysis (PIA) V6.5. The calibration of the data was derived from the Fine Calibration Source (FCS) measurements obtained before and

Table 1. Brightness and fluxes measured for the extended cirrus $\mathrm{MCLD}\,123.5+24.9$ and the $\mathrm{Telephone}$ condensation.

Instrument	λ μm	$\mathrm{MCLD}\,123.5+24.9$ MJy/sr$\pm3\sigma$	Telephone Jy$\pm3\sigma$
IRAS	60	0.12$\pm$0.09	$--$
IRAS	100	4.21$\pm$1.18	1.91$\pm$0.17
PHOT	150	20.22$\pm$4.0	11.3$\pm$3.4
SPM	200	31.0$\pm$5.9	22.4$\pm$4.0
SPM	260	25.7$\pm$5.5	23.3$\pm$5.4
SPM	360	17.0$\pm$2.8	22.8$\pm$5.9
SPM	580	5.1$\pm$1.2	7.6$\pm$5.5

after the observations on the sky. Note that the calibration signal shows no systematic drift for the C200 detector observations so that no "drift handling" was necessary under PIA. The beam of ISOPHOT at $150\,\mu$m is about 2'.

The map obtained at $150\,\mu$m is shown in Fig. 4. The extended cirrus is clearly detected. Two emission peaks are located outside the region covered by the SPM observations. The brightest one, south of the SPM cut at $\alpha_{1950} = 1^{\rm h}43^{\rm m}00.0^{\rm s}$, $\delta_{1950} = 87°24'26''$ ($l = 123.67°$, $b = 24.88°$) corresponds to the H_2CO absorption core labelled H_2CO-B in Großmann and Heithausen (1992). The one lying north of the cut at $\alpha_{1950} = 1^{\rm h}34^{\rm m}14.9^{\rm s}$, $\delta_{1950} = 87°24'57''$ ($l = 123.56°$, $b = 24.86°$) was also apparent in their H_2CO map, although with a lesser contrast. The dark $\mathrm{Telephone}$ nebula now appears as an E-NE extension of the cirrus emission. Note also that some fainter emission is detected at the eastern end of the map.

4. Results

We simulate the SPM observation raster on the 60, 100 and $150\,\mu$m sky by extracting from the IRAS ISSA maps at 60 and $100\,\mu$m and from our ISOPHOT $150\,\mu$m map the brightnesses at each scan position, as it would have been observed with SPM, taking into account the SPM observing positions, beam size and modulation on the sky. The resulting simulated dual beam signal at 60, 100 and $150\,\mu$m is then treated exactly as the SPM data. Individual scans (including the simulated ones) are then deconvolved using standard inverse Fourrier filtering (Emerson et al. 1979) and averaged for each position along the scan. Note that the deconvolution artificially constrains the deconvolved signal to be zero at scan edges. The resulting dual beam and deconvolved average profiles are shown in Fig. 3a and 3b respectively. They are compared to the average simulated IRAS $100\,\mu$m profile scaled to match the intensity of the extended emission (see Sect. 4.1).

It can be seen from Fig. 3 that the large scale shape of the average $100\,\mu$m profile is similar to that observed at longer wavelengths with SPM. Apart from the extended cirrus, the submillimeter emission counterpart of the dark $\mathrm{Telephone}$ nebula seen in B band absorption is now clearly visible in emission in all SPM channels at offset position -0.5' while it is not detected in the ISSA $100\,\mu$m profile. It is also clearly seen in the $150\,\mu$m ISOPHOT profile. Two fainter structures are also detected at offsets -4' and -8'. These positions correspond precisely to the offset locations of the 2 maxima detected in the ISOPHOT map at $150\,\mu$m and the H_2CO cores. Although we did not observed right toward these two condensations with SPM (see Fig. 1), it is likely that the faint maxima detected in the SPM profiles are due to these condensations passing through the lobe of the instrument (roughly 1.5' off-center). Any attempt to derive the spectrum from these two condensations from our SPM data would require knowledge of the beam shape and absolute pointing reconstruction in the cross scan direction to an higher accuracy than is presently available. Instead, we concentrate on the spectrum of the extended cirrus $\mathrm{MCLD}\,123.5+24.9$ and that of the $\mathrm{Telephone}$ nebula in the following.

4.1. *Spectrum of the extended cirrus* $\mathrm{MCLD}\,123.5+24.9$

We derive the spectrum of the extended cirrus by performing a linear correlation between the average deconvolved profile at $100\,\mu$m and the corresponding profiles obtained from the PHOT data at $150\,\mu$m and the SPM data, in a region excluding the 6' offset region around the $\mathrm{Telephone}$ position. The coefficients of the correlation lead to the values given in the first column of Table 1, which have been scaled to match the $100\,\mu$m brightness of $\mathrm{MCLD}\,123.5+24.9$ at its peak position ($-6'$ <offset< $-3'$). The quoted uncertainties for the SPM values reflect the rms dispersion between successive scans, as well as the relative uncertainties between the photometry in the different channels of the instrument (5%) and the formal error derived from the correlation with the $100\,\mu$m emission. Note that the $60\,\mu$m is uncertain because when going to short wavelengths ($\lambda < 100\,\mu$m) the cirrus becomes weaker and an additional component with higher 60/100 fills the region around the cirrus. We have performed a correlation study of IRAS and DIRBE brightnesses over a 7° region around the $\mathrm{MCLD}\,123.5+24.9$ cirrus in a region showing similar brightnesses as the cirrus. We found that the IRAS brightnesses have to be increased by 19% and 1.1% at 60 and $100\,\mu$m respectively to match the better calibrated DIRBE values. The IRAS values in Table 1 have been rescaled accordingly. All values have been colour corrected using the actual filters transmission and a grey body spectrum of the form $I_\nu \propto \nu^\beta B_\nu(T_{\rm d})$ with β and $T_{\rm d}$ derived iteratively with the best fit (values in Table 2). No additional photometry corrections other than those implemented in PIA V6.5 were applied to the PHOT data at $150\,\mu$m, although we are aware that corrective factors might have to be applied to correct for far side lobes evidenced in the PHOT beams and that future versions of the reduction software will likely include an improved treatment of drifts. Given the remaining uncertainties on the absolute calibration of PHOT data, we assigned a 30% uncertainty to this measurement and disregard it in the spectral fits.

The best χ^2 fit to the SPM and IRAS data at $100\,\mu$m, taking into account the uncertainties on each measurement, leads to β =2.2 and $T_{\rm d}$=13.0 K. Note that the high values for the index is mainly imposed by the large rise (by a factor of 8) in surface brightness from $100\,\mu$m to $200\,\mu$m. If the spectral index is forced to 2.0, the best χ^2 fit is obtained for $T_{\rm d}$=13.6 K. Both

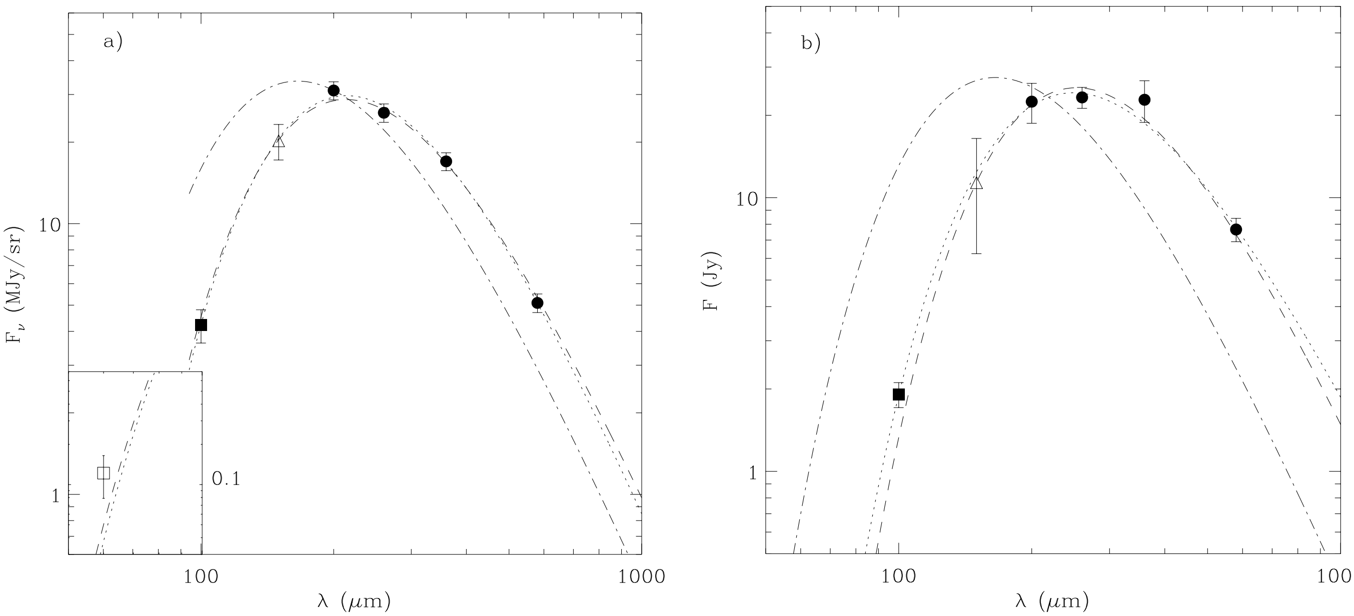

Fig. 5a and b. Spectrum of the extended Polaris cirrus (**a**) and the Telephone (**b**). The data are from IRAS (diamond), ISOPHOT (upper triangle) and SPM (circles). The best χ^2 grey body fit to the data with filled symbols is shown by the dotted line (T_d=13.0 K, $\beta = 2.2$ and T_d=12.9 K, $\beta = 1.54$ respectively). The dashed line is the best fit with $\beta = 2.0$ (T_d=13.4 K and T_d=11.5 K respectively). The dot-dash line shows the spectrum of a typical high latitude cirrus (T_d=17.5 K and $\beta = 2.0$).

spectra are shown on Fig. 5a. The fit with β=2 is barely consistent with the error on the SPM measurement at 200 μm. This is confirmed by the uncertainties on T_d and β reported in Table 1 which corresponds to the 68% confidence level for each individual parameter for the best χ^2 fit. Note that the SPM brightness at 200 and 260 μm appear respectively higher and lower than the best fitted grey body curve. Such a behaviour has been identified previously in several SPM spectra of cold dust condensations. We can exclude that this is due to the contribution of the C^+ cooling line at 158 μm in the SPM 200 μm channel, since this would require a contribution of the line ($\mathrm{C}^+/\mathrm{FIR} \simeq 5\%$) well above the value usually observed in our Galaxy ($\mathrm{C}^+/\mathrm{FIR} \simeq 0.7\%$: Shibai et al. 1991, Wright et al. 1991) or for external galaxies ($\mathrm{C}^+/\mathrm{FIR} = 0.1 - 1\%$: Lord et al. 1996). The effect could also be due to a slight systematic calibration error in our 260 μm channel which has shown to be more sensitive than others to external perturbations. However, we cannot exclude that this might be due to a broad emission or absorption feature in the range 180-300 μm in the emission spectrum of large dust grains in cold regions. Such features could affect our estimate of the dust temperature and the spectral index. For instance, the best χ^2 fit to the data excluding the SPM channel at 200 μm leads to $\beta = 2.08 \pm 0.24$ and T_d=13.7 $\pm$ 0.7 K while excluding the 260 μm channel gives $\beta = 2.3 \pm 0.24$ and T_d=12.7 $\pm$ 0.7 K. These values are within the uncertainties given in Table 2 which we adopt in the following.

In their study of the IR/HI correlation based on COBE data and the recent HI survey from Dwingeloo (Hartmann and Burton 1995), Boulanger et al. (1996) derived a dust effective cross section per H atom $\sigma_\mathrm{H} = 10^{-25}\,(\lambda/250\,\mu\mathrm{m})^{-2}\,\mathrm{cm}^2$, which converts into a dust emissivity at λ=1 mm of $\epsilon_{1\mathrm{mm}} = 7.3\,10^{-34}\,\mathrm{W/H}$ for dust in the diffuse HI medium at high galactic latitude (T_d =17.5 K, $\beta = 2$). This is likely to be more accurate than previous estimates which were based on IRAS data only. In the Rayleigh-Jeans limit, we scale this value to account for the lower value of T_d observed toward $\mathrm{MCLD}\,123.5{+}24.9$ and therefore use $\epsilon_{1\mathrm{mm}} = 5.4\,10^{-34}\,\mathrm{W/H}$ in the following. The total gas column density then writes $N_\mathrm{H} = 6.91\,B_{1mm}\,10^{21}\,\mathrm{H/cm}^2$ where B_{1mm} is the brightness at 1 mm in MJy/sr. In order to derive physical quantities which are directly comparable with the ^{13}CO study of Großmann et al. (1990), we average the IRAS 100 μm emission over the same area on the sky (A=0.157$^{\circ 2}$), which is obtained above the 9.5 MJy/sr level at 100 μm and leads to an average, background subtracted brightness of $B_{100} = 1.36\,\mathrm{MJy/sr}$. Assuming that $\mathrm{MCLD}\,123.5 + 24.9$ as a whole emits according to the spectrum in Fig. 5a, this converts to a mean brightness $B_{1mm} = 0.23\,\mathrm{MJy/sr}$, $N_\mathrm{H} = 1.6\,10^{21}\,\mathrm{H/cm}^2$ (or A_v=0.8 mag), a total gas mass M=24 $\mathrm{M}_\odot$ and a mean gas density $n_\mathrm{H} = 490\,\mathrm{H/cm}^3$. The gas mass derived here from the dust emission is significantly smaller than the mass that Großmann et al. derived from their ^{13}CO data (32 $\mathrm{M}_\odot$). The difference between the two estimates ($\simeq 25\%$) is higher than the uncertainty in our data. It could be due to our assumption that the dust emission spectrum derived here prevails over most of the region detected in ^{13}CO . However, interpreting the mass difference by a change in the dust temperature would require the dust temperature in the area of the cirrus not mapped by SPM to be $T_\mathrm{d} \simeq 10\,\mathrm{K}$. We consider it a more likely hypothesis that the dust emissivity used to derive the dust mass, which was obtained from the IR/HI correlation in the diffuse Galactic medium, is actually too high for a region such as $\mathrm{MCLD}\,123.5 + 24.9$,

Table 2. Physical parameters derived for $\mathrm{MCLD}\,123.5 + 24.9$ and the Telephone.

	$\mathrm{MCLD}\,123.5 + 24.9$		Telephone	
T_d (K)	$13.0^{+0.8}_{-0.7}$	$13.4^{+0.8}_{-0.8}$	$12.9^{+1.4}_{-1.4}$	$11.5^{+1.4}_{-1.4}$
β	$2.2^{+0.27}_{-0.27}$	2.0	$1.54^{+0.45}_{-0.39}$	2.0
N_H $(\mathrm{H/cm^2})$	$1.6\,10^{21}$		$5.1\,10^{22\,\dagger}$	
A_v (mag)	0.8		$26^{\,\dagger}$	
n_H $(\mathrm{H/cm^3})$	490		$6.7\,10^{4\,\dagger}$	
Mass ($\mathrm{M_\odot}$)	24		4.2	

† Average values in a 2' diameter beam.

where the dust is significantly colder. However, a definite conclusion on this important point will have to await the results of a complete mapping of $\mathrm{MCLD}\,123.5 + 24.9$ in the submillimeter.

4.2. *Spectrum of the Telephone nebula*

In order to subtract a realistic baseline corresponding to the extended emission from the cirrus, we use the average deconvolved $100\,\mu\mathrm{m}$ profile which we scale using the average colours of Table 1. Fig. 6 shows the difference as well as the in-scan shape of the SPM beams derived from our Saturn maps. The comparison shows that the Telephone is point-like along the SPM scan direction in the 4 bands. In order to derive the flux of the source, we assume that the same holds in the cross-scan direction. Since only very limited information is available cross-scan at the location of the source in our SPM observations, this hypothesis cannot be tested from our data only. In fact, both the B band extinction patch and the $150\,\mu\mathrm{m}$ PHOT maps indicate that the object is elongated in the S-SW direction. The assumption is therefore likely to underestimate the total flux of the object but should not greatly modify its spectrum since the same assumption is made at all wavelengths. The flux values are reported in Table 1. The quoted error reflects the uncertainty of the SPM measurement as well as the uncertainty on the background subtraction, which we estimated by comparing various baseline subtraction methods. The flux at $100\,\mu\mathrm{m}$ was obtained by coadding all IRAS scans passing through the source, using the SCANPI software available remotely at the Infra-red Processing and Analysis Center (IPAC). The source which has no entry in the IRAS Point Source Catalog or in the Faint Source Catalog but is detected at $100\,\mu\mathrm{m}$ with SCANPI, with a S/N of 5. The flux at $150\,\mu\mathrm{m}$ was computed directly from the map in Fig. 4 from a cut passing through the source at constant elevation, using only the signal away from the extended cirrus (i.e. toward increasing right ascension from the source). This was prefered over using the simulated cuts of Fig. 3 in which the signal from the point source suffered contamination with the extended emission from $\mathrm{MCLD}\,123.5 + 24.9$ and poor baseline subtraction. The comparison of the signal along the ISOPHOT cut with the PSF given in Puget et al. (1999) shows that the Telephone is resolved by the ISOPHOT observations. The resulting spectrum is shown in Fig. 5b.

The best χ^2 fit to the IRAS and SPM data is obtained for $\beta = 1.54$ and $T_\mathrm{d} = 12.9\,\mathrm{K}$. Since the extinction is probably much higher for this object than within the cirrus (see Table 2), the low value of the emissivity index evidenced here could well be due to mixing of contributions from dust at different temperatures along the line of sight. The fact that the apparent dust temperature T_d is of the same order as for the cirrus can also be explained this way, since grey body fits always produce higher temperatures for lower β values. In fact, if the spectrum of the point source is fitted using $\beta = 2$, the temperature becomes $T_\mathrm{d} = 11.5\,\mathrm{K}$ significantly lower than the equivalent value for the extended cirrus ($T_\mathrm{d} = 13.4\,\mathrm{K}$). As for the cirrus spectrum, it can be seen that SPM data-points in the range $180 - 300\,\mu\mathrm{m}$ are not well represented by the modified black-body.

The flux of the Telephone extrapolated to λ =1 mm is $\simeq 1.9\,\mathrm{Jy}$ which corresponds to a brightness averaged in our smallest beam (2' diameter or an equivalent radius of 0.058 pc at 200 pc) of 7.15 MJy/sr. Using the same conversion factor as previously for the cirrus (i.e $5.2\,10^{-34}\,\mathrm{W/H}$ at 1 mm), this leads to an average H column density of $N_\mathrm{H} = 5.1\,10^{22}\,\mathrm{H/cm^2}$ or A_v=26 mag and a mean density of $n_\mathrm{H} = 6.7\,10^4\,\mathrm{H/cm^3}$. Note however that the submillimeter emission of the Telephone is not resolved here, so that the column density and density figures given above should be considered as lower limits. Would most of the submillimeter emission come from the $\mathrm{NH_3}$ core detected by Großmann and Heithausen (1992) (equivalent radius of 0.7'), these figures would have to be increased by a factor of 2. The total mass derived from our observations is $4.2\,\mathrm{M_\odot}$ at a distance of 200 pc. Given the above uncertainties, the physical parameters derived here from our SPM measurements agree reasonably well with those proposed by Großmann and Heithausen from the analysis of their molecular data. Their $\mathrm{C^{18}O}$ data indicated $n_\mathrm{H} \simeq 3.6\,10^4\,\mathrm{H/cm^3}$ and a mass of $2.3\,\mathrm{M_\odot}$ within 0.07 pc while their $\mathrm{NH_3}$ data lead to $n_\mathrm{H} \simeq 8\,10^4\,\mathrm{H/cm^3}$ and $0.74\,\mathrm{M_\odot}$ within 0.04 pc. Our mass estimate is therefore higher than their $\mathrm{C^{18}O}$ mass by a factor of 1.8.

5. Discussion

The data presented in Sect. 4 for the cirrus $\mathrm{MCLD}\,123.5 + 24.9$ indicate a fairly steep dependency of the dust emissivity with wavelength ($\beta = 2.2 \pm 0.27$) which is consistent with the canonical value $\beta = 2$ extrapolated from NIR measurements for 3-D amorphous or crystalline material (Draine and Lee 1984, Emerson et al. 1979, Pollack et al. 1994). Note that Kramers-Kronig relations impose $\beta > 1$ as a physically acceptable limit (Emerson 1979) but that there is no firm physical ground to the common belief that β should satisfy $\beta < 2$. In fact, experimental evidences exist that astrophysically relevant material may have $\beta > 2$. Koike et al. (1995) have noticed that this index for Carbon based compounds increases with the degree of crystallization and have measured values up to $\beta = 2.7$ in the range 60-500 $\mu\mathrm{m}$ at room temperature. The recent laboratory measurements of β in the submillimeter range at low temperatures by Agladze et al. (1996) has shown that the emissivity index of some bulk amorphous silicates precursors such as $\mathrm{MgO.SiO_2}$

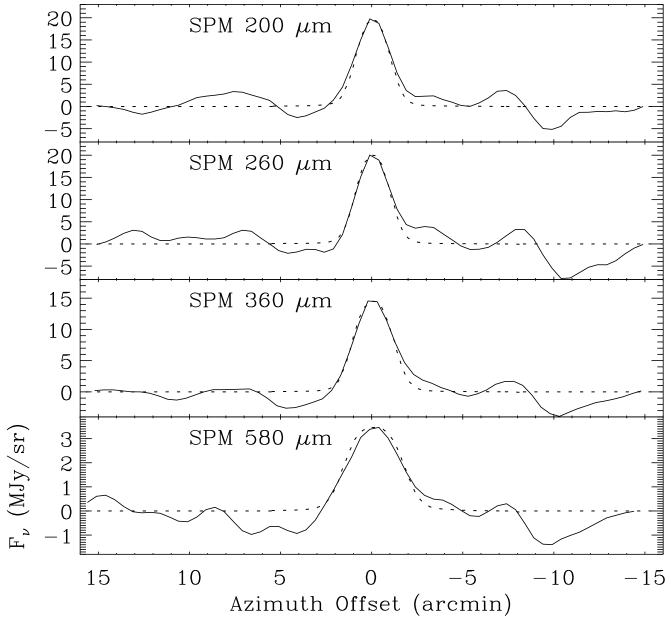

Fig. 6. The solid line shows the profile of the emission from the $\mathrm{Telephone}$ nebula (point source near offset=0) obtained by subtracting the baseline shown in Fig. 3 (see text) in the 4 SPM bands. The dashed line shows the beam shape of the instrument in each band.

and $2\mathrm{MgO.SiO_2}$ strongly varies with temperature and is higher than 2 between $\simeq 5$ and 20 K, reaching $\beta = 2.5$ around 10 K. The SPM/PRONAOS data presented here show that dust emissivity indexes higher than 2 may indeed be present in cold regions of the ISM such as $\mathrm{MCLD}\,123.5 + 24.9$. Unfortunately, most of the uncertainty on our β measurement arises from the behaviour of the spectrum between 200 and 300 μm (see discussion in Sect. 4.1) which departs from a grey body law. Sensitive measurement of $\mathrm{MCLD}\,123.5 + 24.9$ in the millimeter range would greatly help improving the accuracy on β.

In order to assess whether the low temperature measured toward $\mathrm{MCLD}\,123.5+24.9$ can be explained by a decrease of the Inter-Stellar Radiation Field (ISRF), we model the dust emission of the cirrus using a self consistent radiative transfer and dust emission model similar to that used in Bernard et al. (1992). The cirrus is represented by an homogeneous spherical dust and gas condensation with an r^{-2} density distribution, a mean extinction of $A_\mathrm{v} = 0.8$ mag, a diameter of 0.78 pc (corresponding to the surface of the molecular emission region) and a total mass of $24\,\mathrm{M}_\odot$. We used the dust composition and the ISRF adopted by Désert et al. (1990)(DBP) as representative of the local values in the solar neighbourhood. The cirrus is heated from the outside by the ISRF and the local radiation field is computed at each position in the cloud through a standard radiative transfer calculation. The dust emission is calculated according to the model of DBP, which fully takes into account thermal fluctuations of grains and ensures self-consistency between emission and extinction. The output spectra from the model are averaged over a cut though the cloud similar to that observed by SPM/PRONAOS. We then compute the average brightness in the SPM and IRAS filters and perform a least χ^2 fit to the IRAS $100\,\mu\mathrm{m}$ and SPM values in the same way as for actual data with β set to 2. As mentioned earlier, the cirrus $\mathrm{MCLD}\,123.5+24.9$ is part of the large scale Polaris Flare which could contribute a substantial attenuation of the ISRF. We account for the extinction in the flare by using an incident radiation field on the cirrus of the form $ISRF(\lambda) \times \exp(\,-\,\tau_\mathrm{fl}(\lambda)/2)$ in the model, where $\tau_\mathrm{fl}(\lambda)$ is the total extinction through the flare assuming a standard extinction law and a given total extinction of the flare in the visible A_v^fl. We therefore assume that the cirrus is located at the center of the flare in all directions, which probably overestimates the shielding. Fig. 7a shows the apparent dust temperature derived from the fit as a function of A_v^fl. As expected, the dust temperature decreases steadily with A_v^fl, starting from a value slightly lower than the canonical 17.5 K for A_v^fl=0, due to the attenuation within the cloud. It reaches the observed value of 13 K near A_v^fl=4.5 mag and is consistent with our $1-\sigma$ error bar for $A_v^\mathrm{fl} > 3$ mag. Explaining the low dust temperature observed toward $\mathrm{MCLD}\,123.5 + 24.9$ by the attenuation of the radiation field in the flare would therefore require the average visual extinction through the flare to be larger than 3 mag ($N_\mathrm{H} \simeq 6.0\,10^{21}\,\mathrm{H/cm^2}$), so that the region detected by SPM would be screened by Av=1.5 mag in any direction. Note that the above calculations assumed spherical symmetry, homogeneous medium and that $\mathrm{MCLD}\,123.5+24.9$ is located at the center of the flare. This is unlikely true since $\mathrm{MCLD}\,123.5 + 24.9$ is obviously elongated, likely inhomogeneous and not at the center of the flare at least in the plane of the sky (see Fig. 7b). These assumptions tend to underestimate the radiation field intensity, so that the curve in Fig. 7a must be considered a lower limit to the actual dust temperature.

Fig. 7b shows a large scale map of the visible extinction toward the Polaris Flare obtained through star counts in the PMM-USNO catalog (Monet 1996) in the B band, following the procedure described in Cambrésy (1998) and Cambrésy (1999). An adaptive grid with a fixed number of stars per cell (20) is used to perform the counts, so that the resolution of the A_v map varies with position, following the local stellar density. It varies from 4.5’ to 5.2’ in regions of low extinction from the bottom to the top of Fig. 7 due to the Galactic gradient and reaches 5-8’ toward the flare. The counts are then corrected for the variations of the background stellar density with Galactic latitude, in order to take into account the intrinsic Galactic structure. Systematic errors are believed to be < 0.25 mag. It is worth noticing that the method assumes that all stars are located behind the structure producing the extinction, which tends to underestimate the extinction, in particular toward low Galactic latitudes. In the case of the Polaris flare, we estimated from the Galactic model of Besançon Observatory[2] that less than 2% of the stars used in the counts are in fact foreground stars, leading to a negligible extinction correction. The extinction value measured in the map of Fig. 7b for the cirrus $\mathrm{MCLD}\,123.5 + 24.9$ is $\simeq 0.8$ mag which is compatible with the value derived from our submillimeter measurements in Sect. 4.1. In the extended region surrounding $\mathrm{MCLD}\,123.5 + 24.9$, the extinction of the flare is measured to

---

[2] through http://www.obs-besancon.fr/www/modele

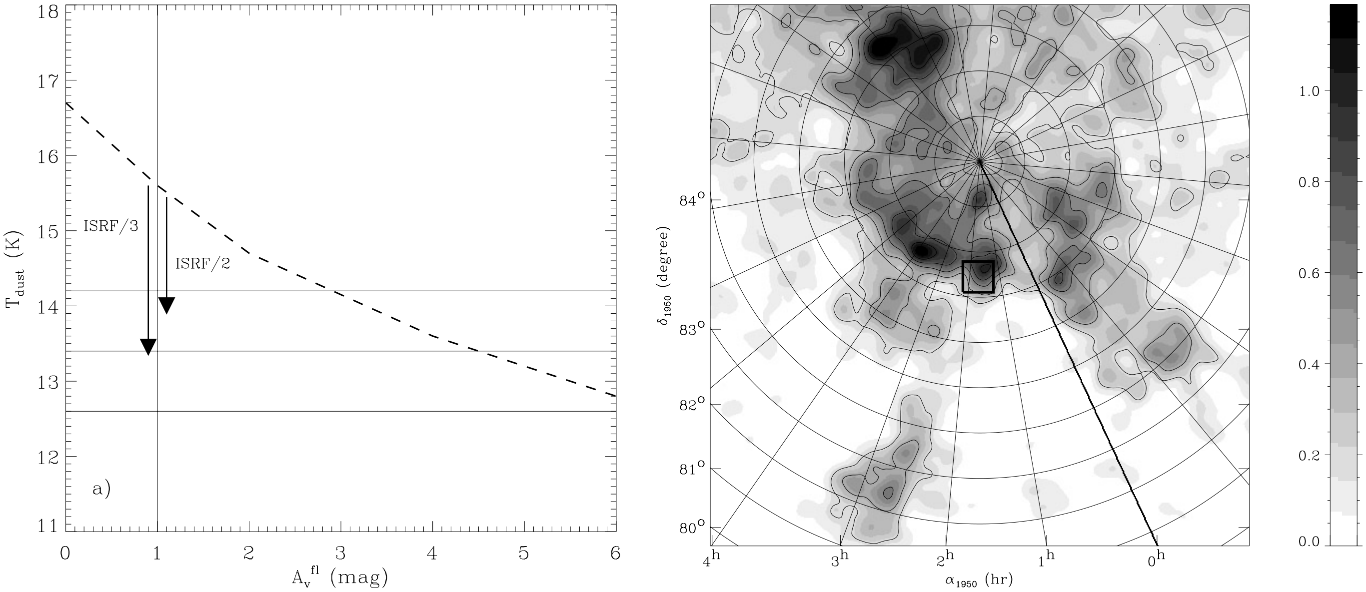

Fig. 7a and b. **a** Apparent dust temperature computed for a dust cloud similar to $\rm MCLD\,123.5+24.9$ (see text) as a function of the total visible extinction of the surrounding flare. The vertical line at $A_v^{\rm fl}$=1 mag shows the upper limit to the observed extinction of the flare. The horizontal lines show the dust temperature observed toward $\rm MCLD\,123.5 + 24.9$ for $\beta = 2$ ($\rm T_d\,=13.4 \pm 0.8K$). The downward arrows show the effect of decreasing the ISRF by a factor of 2 and 3. **b** Map of the visible extinction toward the Polaris Flare (see text). Lower level and level interval is 0.2 mag. The location and size of Fig. 1 is shown by the square symbol.

be < 0.8 mag. We take the elongated geometry of the flare into account to the first order assuming a cylindrical geometry and a similar shape along the line of sight than in the plane of the sky, using the aspect ratio of the contour $A_{\rm v}$=0.4 mag in Fig. 7b. We obtain an effective $A_{\rm v}$ through the flare $A_v^{\rm fl}$ <1.0 mag. This value is much lower than required ($A_{\rm v}$ >3 mag). Therefore, the extinction through the flare is too low to explain the low dust temperature observed toward $\rm MCLD\,123.5 + 24.9$.

In principle, the low dust temperature could also result from the local ISRF being weaker than in the solar neighbourhood, due to a lack of stars in the Polaris area. Using the same method as above, we derive that a global decrease of the ISRF by a factor of 2-3, in addition to the extinction provided by the flare (using $A_v^{\rm fl}$= 1 mag) would be necessary to explain the observed temperature. Such a variation of the ISRF strength over a 200 pc scale is unlikely: The diffuse sky light in the red and blue toward the Northern Celestial Pole (NCP) region which contains the Polaris Flare has been measured by Pioneer away from most of the contamination by zodiacal emission (see Fig. 3c in Toller et al. 1987). Their Table 1 shows that the diffuse emission from the NCP is consistent, within $\simeq 15\%$, with the median value of the other regions observed by Pioneer toward the ecliptic and galactic poles, the only region showing a significantly higher brightness being the South Celestial Pole, due to the presence of the Magellanic clouds. Since this median value is representative of the solar neighbourhood ISRF intensity, the good agreement with the NCP value shows that the local ISRF strength in the Polaris region is likely similar to that in the solar neighbourhood. We conclude that the factor of 2-3 decrease needed can be ruled out by the observations in the visible where large grains absorb most of their energy.

We therefore conclude that neither the extinction nor local variations of the ISRF intensity can explain the low temperature observed toward $\rm MCLD\,123.5 + 24.9$. As mentioned earlier, the cirrus $\rm MCLD\,123.5 + 24.9$ exhibits unusually low values of the 60/100 IRAS colour ratio. In the frame of dust models which take transient heating of small dust particles into account, this is taken to indicate a lack of Very Small Grains (VSG) which dominate the $60\,\mu\rm m$ emission over the larger size grains which contribute most of the $100\,\mu\rm m$. Fig. 5 shows that the $60\,\mu\rm m$ emission toward $\rm MCLD\,123.5 + 24.9$ falls somewhat above the best fit to the BG emission at $\lambda > 100\,\mu\rm m$. From the amplitude of the excess, we derive, using DBP model that $\simeq 30 - 50\%$ of the VSG (size 1.2-15 nm) could be missing from the dust distribution. Detailed models of dust behaviour in turbulent medium (see for instance Ossenkopf 1993) indicate that the smallest dust grains can coagulate or get adsorbed at the surface of larger grains, thus forming fluffy aggregates. The resulting fractal grains generally have increased emissivity in the FIR (e.g. Wright 1987, Bazel and Dweck 1990) which will tend to lower their equilibrium temperature. Dust coagulation could therefore provide a natural explanation both to the reduced abundance of VSG and to the low dust temperature observed toward $\rm MCLD\,123.5 + 24.9$. Such a detailed modelling of dust coagulation is clearly beyond the scope of the present paper, and it remains to be demonstrated that this process could be efficient enough to produce large aggregates in the low density environments such as the cirrus cloud studied here ($n_{\rm H} \simeq 500\,\rm cm^{-3}$). As mentioned earlier, the submillimeter observations presented in this paper indicated no departure from a λ^{-2} dust emissivity law, which would also have to be accounted for by such a model. Dedicated numerical simulations as well as additional observations of the dust continuum, in particular at longer wavelength, are clearly required to test if dust aggregation could explain the observations.

6. Conclusion

We have presented observations of the $\mathrm{MCLD}\,123.5+24.9$ cirrus cloud in the Polaris Flare, obtained with the submillimeter balloon-borne experiment SPM/PRONAOS. These sensitive measurements allow for the first time to study the submillimeter emission from large dust grains at the scale of a few arc minutes toward cirrus clouds. We have unambiguously detected the extended emission from the cirrus along a narrow strip in the four photometric channels of the instrument from 200 to $600\,\mu\mathrm{m}$. We also evidenced the point-like emission counterpart of a denser structure of the cirrus (so called $\mathrm{Telephone}$ nebula) which was first detected as an NH_3 clump and appears as a prominent extinction region in CCD B-band images.

The dust mass derived for the extended cirrus $\mathrm{MCLD}\,123.5+24.9$ is smaller than its molecular mass. This may indicate a dust emissivity value lower than the average in the diffuse ISM by about 25%. However a full mapping of the cirrus in the submillimeter is required before this can be fully demonstrated. The spectrum of the extended cirrus indicates a low dust temperature ($T_\mathrm{d}=13\,\mathrm{K}$) and a steep dust emissivity index ($\beta=2.2$). Within the uncertainty, the dust emissivity index value is barely consistent with that measured toward the average diffuse medium ($\beta=2$). It is possible that the measurements presented here provide the first observational evidence for dust emissivity indexes larger than 2 in cold ISM clouds, as was measured recently in the laboratory for silicate material at low temperature.

Although the visual extinction across $\mathrm{MCLD}\,123.5+24.9$ is less than 1 mag, the dust equilibrium temperature observed (13 K) is much smaller than that of large grains heated by the average solar neighbourhood ISRF (17.5 K). We have investigated in details the possible origins for such a low dust temperature. The total extinction across the Polaris Flare is too low to explain the observed temperature by the absorption of the heating radiation field. A local minimum of the ISRF combined to extinction effect can also be excluded. We conclude that the low dust temperature in $\mathrm{MCLD}\,123.5+24.9$ must be caused by a change of the optical properties (absorption and/or emission) of large dust grains compared to those derived for the average diffuse ISM in our Galaxy. The very low 60/100 IRAS colour ratio observed toward $\mathrm{MCLD}\,123.5+24.9$ and the Polaris Flare in general indicates a lack of very small dust grains. We suggest that the change of optical properties causing the low dust temperatures may result from the adsorption of small dust particles onto the surface of larger size grains.

Acknowledgements. We are indebted to the CNES team led by F. Buisson who ensured the development and operations of the PRONAOS gondola and telescope. We are also grateful to the NSBF team lead by D. Ball who made the successful flight possible and to the CNRS team lead by G. Guyot who was in charge of the focal plane instrument SPM. We would like to thank Pr. Heithausen for very helpful comments on the manuscript.

References

Agladze N.I., Sievers A.J., Jones S.A., Burlitch J.M., Beckwith S.V.W., 1996, ApJ 462, 1026
Bazel D., Dweck E., 1990, ApJ 360, 142
Bernard J.P., Boulanger F., Désert F.X., Puget J.L., 1992, A&A 263, 258
Boulanger F., Abergel A., Bernard J.P., et al., 1996, A&A 312, L256
Buisson F., Ristorcelli I., Berrivin S., et al., 1997, In: Proceedings of the IAF conference, Turino
Cambrésy L., Epchtein N., Copet E., et al., 1997, A&A 324, L5
Cambrésy L., 1998, In: Epchtein N. (ed.) The Impact of Near Infrared Sky Surveys on Galactic and Extragalactic Astronomy. ASSL series Vol. 230, Kluwer Academic Publishers, p. 157
Cambrésy L., 1999, Accepted for A&A
Désert F.X., Boulanger F., Puget J.L., 1990, A&A 237, 215
Draine B.T., Lee H.M., 1984, ApJ 285, 89
Emerson D.T, Klein U., Haslam C.G.T., 1979, A&A 76, 92
Falgarone E., Panis J.F., Heithausen A., et al., 1998, A&A 331, 669
Grenier I.A., Lebrun F., Arnaud M., Dame T.M., Thaddeus P., 1989, ApJ 347, 231
Großmann V., Heithausen A., Meyerdierks H., Mebold U., 1990, A&A 240, 400
Großmann V., Heithausen A., 1992, A&A 264, 195
Hartmann D., Burton W.B., 1995, Atlas of the Galactic HI emission. Cambridge University Press
Heithausen A., Thaddeus P., 1990, ApJ 353, L49
Heithausen A., Stacy J.G., de Vries H.W., Mebold U., Thaddeus P., 1993, A&A 268, 265
Koike C., Kimura S., Kaito C., et al., 1995, ApJ 446, 902
Lagache G., Abergel A., Boulanger F., Puget J.L., 1998, A&A 333,709
Lamarre J.M., Pajot F., Torre J.P., et al., 1994, IR Phys. Techno. Vol. 35, no2/3, pp277-289
Lemke D., Klaas U., Abraham P., et al., 1996, A&A 315, L64
Lord S.D., Malhotra S., Lim T., et al., 1996, A&A 315, L117
Monet D., 1996, BAAS 188, 5404
Ossenkopf V., 1993, ApJ 280, 617
Pajot F., et al., 1999, in preparation
Pollack J.B., Hollenbach D., Beckwith S., et al., 1994, ApJ 421, 615
Puget J.L., Abergel A., Bernard J.P., et al., 1996, A&A 308, L5
Puget J.L., Lagache G., Clements D.L., et al., 1999, accepted in A&A
Ristorcelli I., Serra G., Lamarre J.M., et al., 1998, ApJ 296, 467
Reach W.T., Dweck E., Fixsen D.J., et al., 1995, ApJ 451, 188
Shibai H., Okuda H., Nakagawa T., et al., 1991, ApJ 374, 522
Toller G., Tanabe H., Weinberg J.L., 1987, A&A 188, 24
Wright E.L., 1987, ApJ 320,818
Wright E.L., Mather J.C., Bennett C.L., et al., 1991, ApJ 381, 200
Zagury F., et al., 1999, in preparation